Inverse design of an isotropic suspended Kirchhoff rod: theoretical and numerical results on the uniqueness of the natural shape

Florence Bertails-Descoubes, Alexandre Derouet-Jourdan, Victor Romero, Arnaud Lazarus

Inverse design of an isotropic suspended Kirchhoff rod: theoretical and numerical results on the uniqueness of the natural shape

Florence Bertails-Descoubes[*†‡] Alexandre Derouet-Jourdan[*§]
Victor Romero [†] Arnaud Lazarus[¶]

Author version
Received December 1st, 2017
Published April 1st, 2018 at the Roy. Soc. Proc. A

Abstract

Solving the equations for Kirchhoff elastic rods has been widely explored for decades in mathematics, physics and computer science, with significant applications in the modeling of thin flexible structures such as DNA, hair, or climbing plants. As demonstrated in previous experimental and theoretical studies, the natural curvature plays an important role in the equilibrium shape of a Kirchhoff rod, even in the simple case where the rod is isotropic and suspended under gravity. In this paper, we investigate the reverse problem: can we characterize the natural curvature of a suspended isotropic rod, given an equilibrium curve? We prove that although there exists an infinite number of natural curvatures that are compatible with the prescribed equilibrium, they are all equivalent in the sense that they correspond to a unique natural shape for the rod. This natural shape can be computed efficiently by solving in sequence three linear initial value problems, starting from any framing of the input curve. We provide several numerical experiments to illustrate this uniqueness result, and finally discuss its potential impact on non-invasive parameter estimation and inverse design of thin elastic rods.

[*]Joint first authors
[†]Univ. Grenoble Alpes, Inria, CNRS, Grenoble INP, LJK, 38000 Grenoble, France
[‡]Florence.Descoubes@inria.fr
[§]OLM Digital Inc., Mikami Bldg. 2F, 1-18-10, Wakabayashi, Setagaya, Tokyo, 154-0023, Japan
[¶]Sorbonne Universités, UPMC Univ Paris 06, CNRS, UMR 7190, Institut Jean Le Rond d'Alembert, F-75005, Paris, France

1 Introduction

Long and thin flexible structures, alternately called *strands*, *filaments*, *threads*, or *fibers* — and we shall use the latter name in this paper — are well spread in our environment. It is actually striking to note that such one-dimensional structures represent a large body of physical, biological and manufactured phenomena at the macroscopic scale, such as hair fibers, plant stems, or cables, but also at much smaller scales, such as macromolecules or carbon nanotubes. In many cases, fibers are not naturally straight but feature an intricate *natural shape*, which may be for instance wavy or curly. For small strains and when not overly constrained, their deformation is dominated by *bending* and *twisting* elastic deformations, while stretching and shearing can be neglected. Due to geometric nonlinearities, fibers are prone to large displacements and instabilities, such as buckling. The diversity and complexity of the resulting shapes greatly contribute to the structural richness of the real world.

Kirchhoff's theory for thin elastic rods Equations for inextensible and unshearable elastic fibers were first developed by Kirchhoff and Clebsch in their theory of thin elastic rods under finite displacements [1, 2]. Within a more general framework on shells, rods and points, the Cosserat brothers [3] later on proposed a clever mathematical representation of the rod geometry: the rod was described as a space curve, namely the *centerline*, together with a *material* frame attached to the cross-section of the rod and continuously rotating along the centerline about the so-called *Darboux* rotation vector. A modern description of these theories can be found in [4, 5].

In the past, a large body of research has been devoted to the analytical study and numerical solving of the Kirchhoff rod equations, for a diverse set of applications ranging from the understanding of DNA supercoiling [6, 7, 8] and climbing plants [9, 10] to the simulation of submarine cables [11, 12], surgery threads and needles [13, 14], and hair [15, 16]. In all these problems, it has especially been shown that taking the natural curvature[1] into account has a great impact on the equilibrium states of a fiber, see for example [17, 18] for an analytical and numerical writhing model or [19] for experiments. Particular cases such as a suspended fiber under gravity or a coiling fiber on a rigid substrate have been studied theoretically and experimentally in [20] and in [21], respectively.

In this paper, we are concerned with the reverse problem: how can the natural curvature of a fiber be characterized, given one equilibrium configuration? More precisely, given an arbitrary space curve, how can it be interpreted as the centerline of a Kirchhoff rod at equilibrium? When material parameters are fixed, what are the conditions that should be satisfied by the natural curvature of the corresponding rod? Does a natural curvature field meeting these conditions always exist, and if yes, is it unique? Our main contribution here is to show that, in the case of an suspended isotropic fiber under gravity, any input

[1] The term *curvature* is used here for the sake of simplicity. In the following we shall rather talk about *material strains*, which includes the material twist and the material curvatures of the rod.

curve determines a unique natural shape (corresponding to *equivalent* natural curvature fields), regardless of the infinite set of admissible material frames for the input curve.

Inverse static design The problem we investigate belongs to the class of so-called *inverse design* problems, where material parameters are known and one is looking for the natural (or intrinsic) shape of an object. This is in contrast to *inverse measurement* problems, where material properties are searched for [22]. In particular, we focus on an inverse *static* problem, where the only available information is a shape of our object at equilibrium under gravity.

Different communities, from Applied Mathematics and Mechanics to Computer Graphics, have been conducting analytical and numerical studies for solving inverse problems in structural mechanics, and a good introduction to these is given in [23]. More specifically, a number of studies have been conducted in the case of *elastic* materials. On the one hand, some deep mathematical analyses of continuous systems were performed, mostly to identify material parameters such as Young moduli of arbitrary objects [24] or geometric properties such as the cross-sectional area or the second moment of inertia of a beam [25]. Such analytical approaches were however limited to the context of linear elasticity. On the other hand, numerical approaches have been explored to tackle inverse problems related to more general, nonlinear systems. These methods were in particular applied to the inverse design of mass-spring systems [26] and FEM models [27, 28, 29], with some applications to the fabrication of compliant mechanisms [30, 31]. The connection between these numerical approaches is that they all use a *nodal* discretization of the system, i.e., both the deformed and natural shapes are described by 3D positions. The resulting inverse problem is thus nonlinear and is classically solved using a Newton-Raphson approach, potentially combined with continuation techniques [29]. However, a solution may not always exist for arbitrary input shapes, and one may prefer to relax the problem using a least-squares formulation [32], which consists in minimizing the misfit between the model prediction (computed by simulation) and the input data. Anyway, in all cases one is faced with two major issues. First, as the misfit function is non convex and possibly of very large size, local optimization methods may often be computationally expensive, or worse may simply fail to find the global minimum (similarly, the Newton method may fail to find a solution even if it exists), while global optimization may be too costly to be employed. Second, if it succeeds, such a straight numerical treatment provides only a single solution to the (under-determined) inverse problem and does not give any insight about the general structure of the subspace of solutions.

In some early works, authors of this paper have shown that in the case of a discrete Kirchhoff rod, a nonlinear formulation proves to be unnecessarily complex for inverting the rod under gravity. Indeed, when relying upon a discrete rod model parameterized by *curvatures*, such as the super-helix model [15], the inverse static design problem boils down to a simple linear system to be solved [33, 34]. However, some preliminary step needs to be performed for con-

verting the input curve into the geometry of the discrete model — a piecewise helix in the case of the super-helix model [35]. Though appealing, this approach still remains very dependent on the underlying discrete model, and does not easily extend to other discrete systems. Moreover, although the natural curvature field is unique once the actual curvature field has been computed, there is no guarantee that the geometric conversion step yields a unique actual curvature field from the input curve. This conversion step becomes particularly ambiguous when refining the number of elements — each element becoming straighter and straighter —, preventing the treatment of the limit (continuous) case. Thus no conclusion can be drawn w.r.t. the uniqueness of the natural shape, neither on the discrete nor on the continuous model.

In this paper, we examine the strong, *continuous* equations of Kirchhoff, independently of any discrete scheme. We prove that although there exists an infinity of natural curvature fields satisfying the equilibrium of the input curve, all these different solutions are actually *equivalent*, in the sense that they determine a *unique* natural configuration, up to a rigid motion. This natural shape can be computed efficiently by solving in sequence three linear initial value problems, starting from any framing of the input curve. The benefit is not only the design of a simple, fast and robust inversion procedure, but also a better characterization of the whole space of solutions, which opens the way for a reliable parameter identification process for fibers in the short term.

Framework In this work we restrict ourselves to the study of a static Kirchhoff rod that is clamped at one end while the other end is free. Moreover, the rod is subjected to some known external force field such as gravity. We further assume that the rod is homogeneous and isotropic in both material and geometric ways, that is, material parameters (Young modulus, linear mass density) are uniform and the geometry of the cross-section is circular and uniform. Although limiting, these assumptions remain reasonable when studying particular cases of real thin elastic rods such as plant stems or hair fibers. We discuss potential extension of our work to more general systems in conclusion.

Organization of the paper The paper is organized as follows. In Section 2 we recall the equations for the equilibrium of a Kirchhoff rod. In Section 3 we specify all the possible framings of an input curve Γ, and establish the exact relationship between the curvature vector fields of two equivalent material frame fields. Section 4 is the central part of our paper, as it proves the uniqueness of the natural shape of a Kirchhoff rod whose centerline matches the input curve Γ at equilibrium under gravity. In Section 5 we describe a simple numerical algorithm for computing this unique natural shape, and illustrate our uniqueness result through several numerical experiments. Finally, we discuss in Section 6 the limitations and the scope of our theoretical and numerical contributions, before concluding.

2 Background: equilibrium of a Kirchhoff rod

Before tackling our inverse design problem, we recall here the fundamental principles governing the equilibrium of a Kirchhoff rod.

Let $SO(3)$ be the group of 3D rotations and $\mathcal{C}^n_{(E,F)}$ the set of functions from E to F that are n times continuously differentiable. We consider an inextensible and unshearable material rod of length L, represented by a centerline $\Gamma \in \mathcal{C}^3_{([0,L],\mathbb{R}^3)}$, together with a material frame $\mathcal{R} \in \mathcal{C}^2_{([0,L],SO(3))}$, both parameterized by arc length $s \in [0, L]$. At location s, the vector $\Gamma(s)$ gives the 3D position of the centerline; the rotation $\mathcal{R}(s)$, represented as the set of three vectors of $\mathbb{R}^3$, $\mathcal{R}(s) = \{\mathbf{n}_0(s), \mathbf{n}_1(s), \mathbf{n}_2(s)\}$, encodes the frame attached to the cross-section of the rod. As the rod is assumed to be inextensible and unshearable, the frame $\mathcal{R}(s)$ is orthonormal and *adapted* to the centerline $\Gamma(s)$, so that its first vector coincides with the tangent of the curve[2],

$$\forall s \in [0, L] \quad \mathbf{n}_0(s) = \Gamma'(s) \tag{1}$$

while the two vectors $\mathbf{n}_1(s)$ and $\mathbf{n}_2(s)$ are attached to the cross-section of the rod, which is orthogonal to the tangent (see Figure 1a). We further assume that the rod is clamped at $s = 0$ with prescribed clamped position $\Gamma(0) = \Gamma_0$ and orientation $\mathcal{R}(0) = \mathcal{R}_0$, while the end of the rod $s = L$ is free.

2.1 Kinematics

From $s = 0$ to $s = L$, the material frame $\mathcal{R}(s)$ continuously evolves along the centerline $\Gamma(s)$ through infinitesimal rotations about the so-called *Darboux vector* $\mathbf{\Omega}(s) \in \mathcal{C}^1_{([0,L],\mathbb{R}^3)}$ which represents the instantaneous space rotation vector of the rod. This space evolution mathematically writes

$$\forall s \in [0, L] \quad \mathcal{R}'(s) = [\mathbf{\Omega}(s)]_\times \, \mathcal{R}(s), \tag{2}$$

where $[\mathbf{u}]_\times$ denotes the skew symmetric matrix corresponding to the vector cross product operator, i.e., $[\mathbf{u}]_\times \mathbf{v} = \mathbf{u} \times \mathbf{v}$ for all $\mathbf{u}, \mathbf{v} \in \mathbb{R}^3$. The local coordinates of $\mathbf{\Omega}(s)$ in the material frame, denoted by $\kappa(s) \in \mathbb{R}^3$, represent the *material strains* of the rod. More precisely, we have $\mathbf{\Omega}(s) = \mathcal{R}(s)\,\kappa(s)$ with $\kappa(s) = [\kappa_0(s), \kappa_1(s), \kappa_2(s)]$, where $\kappa_0(s) \in \mathcal{C}^1_{([0,L],\mathbb{R})}$ stands for the *material twist* and $\kappa_1(s) \in \mathcal{C}^1_{([0,L],\mathbb{R})}$ and $\kappa_2(s) \in \mathcal{C}^1_{([0,L],\mathbb{R})}$ for the *material curvatures* of the rod. By noticing that for any rotation matrix $R \in SO(3)$ the following property holds,

$$\forall \mathbf{u} \in \mathbb{R}^3, \quad [R\,\mathbf{u}]_\times \; R = R \; [\mathbf{u}]_\times \,, \tag{3}$$

we can reformulate Equation (2) as

$$\forall s \in [0, L] \quad \mathcal{R}'(s) = \mathcal{R}(s)\,[\kappa(s)]_\times \,. \tag{4}$$

[2]This is known as the Euler-Bernoulli condition. It encodes the incompressibility and no shear conditions of the rod, and couples the frame to the centerline.

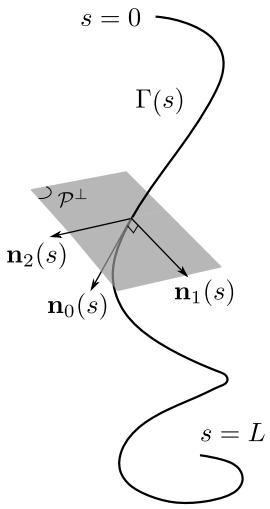

(a) Adapted frame to $\Gamma(s)$

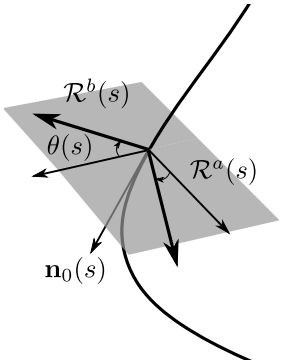

(b) Two different material frames adapted to $\Gamma(s)$

Figure 1: (a) A Kirchhoff rod is kinematically described as a 3D curve $\Gamma(s)$ together with a material frame $\mathcal{R}(s)$, which is adapted to $\Gamma(s)$. (b) An arbitrary curve $\Gamma(s)$ may be framed by an infinite number of adapted material frames; given one candidate frame $\mathcal{R}^a(s)$, another candidate frame $\mathcal{R}^b(s)$ can be parameterized by the rotation angle $\theta(s)$ made from $\mathcal{R}^a(s)$ to $\mathcal{R}^b(s)$ about the tangent vector $\mathbf{n}_0(s)$.

Finally, by compacting the centerline and the material frame into one single function $\mathcal{F} = \{\Gamma; \mathcal{R}\} \in \mathcal{C}^3_{([0,L],\mathbb{R}^3)} \times \mathcal{C}^2_{([0,L],SO(3))}$ and assuming the κ function is fixed, the full kinematics of the rod can be formulated as an explicit[3] linear first-order Cauchy-Lipschitz problem, referred to as the *Darboux problem* (see, e.g., [36]),

$$\begin{cases} \forall s \in [0,L] \quad \mathcal{F}'(s) &= \left\{\mathbf{n}_0(s)\ ;\ \mathcal{R}(s)\left[\kappa(s)\right]_\times\right\} \\ \qquad \text{with} \quad \mathcal{F}(0) &= \{\Gamma_0\ ;\ \mathcal{R}_0\} \text{ as initial conditions,} \end{cases} \tag{5}$$

which admits a unique solution. Note that the ambient space is not a vector space but rather a *nonlinear* differentiable manifold, since the kinematic relationship for the material frame operates onto the non commutative Lie group $SO(3)$. Due to non commutativity, the solution has no formal expression in the general case.

From Γ to κ and from κ to Γ As a result of System (5), any framed curve $\mathcal{F} = \{\Gamma; \mathcal{R}\}$ satisfying (5) may be equivalently described as the set

$$\mathcal{F} = \{\Gamma \in \mathcal{C}^3_{([0,L],\mathbb{R}^3)}; \mathcal{R} \in \mathcal{C}^2_{([0,L],SO(3))},\ \text{s.t. } \mathbf{n}_0(s) = \Gamma'(s)\ \forall s \in [0,L]\},$$

[3]Coefficient of the highest derivative is 1.

or, relying on the material strains, as the simpler (unconstrained) set

$$\mathcal{F} = \{\Gamma_0 \in \mathbb{R}^3; \mathcal{R}_0 \in SO(3); \kappa \in \mathcal{C}^1_{([0,L],\mathbb{R}^3)}\}.$$

In the following, we shall make use of these two equivalent representations. Note however that for the sake of simplicity, the first one will be abbreviated as $\{\Gamma; \mathcal{R}\}$, assuming that $\mathcal{R}$ is implicitly adapted to Γ.

Conversely, the knowledge of the material frame field $\mathcal{R}$ unequivocally determines the Darboux vector field $\mathbf{\Omega}$, and thus the material strain vector field κ. However, an infinite number of material frame fields $\mathcal{R}$ may be constructed from a single input curve Γ, since the only requirement is that one vector of the frame match the tangent of the curve (see Figure 1b). In Section 3, we parameterize the set of material frame fields adapted to a given curve Γ, and establish an equivalency condition on the respective strain vector fields.

2.2 Statics

Let ρ be the volumetric mass density of the rod and S the surface area of its cross-section. We assume the rod is only subjected to known external forces such as gravity. Expressing the balance of linear and angular momentums on an infinitesimal portion of the rod and neglecting inertial momentum due to the vanishing cross-section lead to the following static equations for a Kirchhoff rod,

$$\begin{cases} \mathbf{T}'(s) + \mathbf{p}(s) = \mathbf{0} & \text{(6a)} \\ \mathbf{M}'(s) + \mathbf{n}_0(s) \times \mathbf{T}(s) = \mathbf{0} & \text{(6b)} \end{cases}$$

where $\mathbf{p}$ is the linear density of external forces (for instance, in the case of gravity, $\mathbf{p} = -\rho S g \mathbf{e_z}$) and $\mathbf{T}(s)$ and $\mathbf{M}(s)$ are the internal forces and moments respectively, transmitted from the free part of the rod through its cross-section at s.

Elastic constitutive law Let E be the Young modulus of the rod, μ its shear modulus, and I_0, I_1 and I_2 its torsional and bending momenta, respectively. Static equations are completed with a constitutive law that expresses the ability of the rod to bend and twist elastically,

$$\forall s \in [0, L], \quad \mathbf{M}(s) = \mathcal{R}(s)\, \mathbb{K}_3\, (\kappa(s) - \bar{\kappa}(s))\,, \tag{7}$$

where $\mathbb{K}_3 = \mathrm{diag}_3\,(\mathcal{K}_0, \mathcal{K}_1, \mathcal{K}_2)$ is a diagonal 3×3 matrix collecting the twisting and bending stiffnesses $\mathcal{K}_0 = \mu I_0$, $\mathcal{K}_1 = EI_1$, and $\mathcal{K}_2 = EI_2$ respectively, and where $\bar{\kappa}(s) \in \mathbb{R}^3$ collects the natural strains of the rod, used to model natural "curliness", i.e., the shape the rod would take in the absence of external forces, which is not necessarily straight[4]. As we are modeling a homogeneous material,

[4]However, as we show in this paper, natural curvatures are not an intrinsic quantity for the rod since their value depends on the underlying framing of the rod. For an isotropic and clamped curve, the natural curliness of the rod is actually better characterized by the unformed configuration $\bar{\Gamma}$ of the rod, which is independent of any framing as we demonstrate here. When they are computable, the Frenet curvature and torsion also form an intrinsic parameterization of the natural curliness.

both the linear mass density ρS and the stiffness matrix $\mathbb{K}_3$ are assumed to be constant. In contrast, the natural strain vector $\bar{\kappa}(s)$ may vary spatially to account for a wide range of natural shapes. Finally, we consider here the case of a circular cross-section only (isotropic cross-section), coupled to an isotropic material, meaning that $\mathcal{K}_0 = \frac{\pi}{2}\mu\, a^4$ and $\mathcal{K}_1 = \mathcal{K}_2 = \frac{\pi}{4}E\, a^4$, where a is the radius of the cross-section.

Boundary conditions As mentioned earlier, we consider the rod to be clamped at $s = 0$ and free at the end $s = L$. Corresponding boundary conditions read

$$\begin{cases} \Gamma(0) = \Gamma_0 & \text{Enforced clamped position} \quad (8a) \\ \mathcal{R}(0) = \mathcal{R}_0 & \text{Enforced clamped frame} \quad (8b) \\ \mathbf{T}(L) = 0 & \text{No external force at free end} \quad (8c) \\ \mathbf{M}(L) = 0 & \text{No external torque at free end.} \quad (8d) \end{cases}$$

2.3 Direct vs inverse problem

To the best of our knowledge, equilibria of a Kirchhoff rod have been only studied in the *direct* way, that is, assuming that all parameters — natural strain vector field $\bar{\kappa}$, linear mass ρS, stiffness $\mathbb{K}_3$ — are known, while the geometric configuration Γ of the rod at equilibrium is unknown (as well as the material frame $\mathcal{R}$). In that way, Equations (5–7) together with the boundary conditions (8a) at $s = 0$ and $s = L$ form a nonlinear and stiff boundary value problem, which has no explicit solution in the general case and is known to be difficult to solve numerically. In particular, such a system is known to be prone to bifurcations, that is, multiple equilibria may coexist for a fixed set of parameters and their number may vary function of the parameters.

In contrast, in this paper we examine the reverse way, where only the centerline Γ of the rod at equilibrium is known (not the material frame), whereas parameters of the rod are unknown. More precisely, we are interested in the *inverse design* problem for Kirchhoff rods, consisting in identifying the *natural* strain vector field $\bar{\kappa}$ of a Kirchhoff rod at equilibrium from its geometric configuration Γ. Compared to the direct problem, the inverse problem turns out to be much simpler to study and solve for, as it boils down to a linear IVP of first order (see Section 4). However, the choice of the initial framing of the input curve Γ has an impact on the natural strain vector field that is solution to the inverse problem. The fundamental result of this paper is to show that all these different solutions are actually equivalent, in the sense that they determine the same natural configuration $\bar{\Gamma}$, up to a rigid motion.

Before considering the mechanical equations of our inverse problem in Section 4, we provide more geometric insight to the problem in Section 3, by characterizing how for the same curve two different sets of framings relate to each other.

3 Equivalent framings of a geometric curve

In this section we see how to transform a merely geometric curve Γ into a *framed* curve, i.e., a material rod composed of a centerline Γ *and* an adapted material frame field $\mathcal{R}$. While the input curve only carries geometric information, the material rod carries some mechanical information, such as how matter deforms along the centerline. The key result of this section is to establish the exact relationship between the strain vector fields κ^a and κ^b related to two different framings $\mathcal{R}^a$ and $\mathcal{R}^b$ of the input curve Γ.

Let Γ be a smooth curve of length L parameterized by its arclength $s \in [0, L]$. At this stage, required degree of smoothness varies upon the material frame field that is chosen. For instance, if the Frenet frame is chosen, as we do later, at least C^3-continuity is required to define torsion as a continuous function of s (provided curvature does not vanish), allowing us to interpret the Frenet frame as a C^1-smooth material frame. For this reason, we assume as in Section 2 that Γ is at least C^3-smooth, that is, $\Gamma \in \mathcal{C}^3_{([0,L],\mathbb{R}^3)}$.

3.1 Framing a space curve

The idea is to equip Γ, which is a merely geometric curve, with an orthonormal and adapted material frame field $\mathcal{R} = (\mathbf{n}_0 = \Gamma', \mathbf{n}_1, \mathbf{n}_2) \in \mathcal{C}^2_{([0,L],SO(3))}$. Given such a frame field, there exists a Darboux vector field $\mathbf{\Omega} \in \mathcal{C}^1_{([0,L],\mathbb{R}^3)}$ which corresponds, at each location s, to the instantaneous rotation vector of the frame $\mathcal{R}(s)$, i.e., such that Equation (2) holds. From the Darboux vector field, we may finally define a strain vector field $\kappa = (\kappa_0, \kappa_1, \kappa_2)$ which satisfies Equation (4).

Classical examples of material frames The *Frenet frame* is a material frame which admits the Darboux vector $\mathbf{\Omega}^f(s) = \tau_g(s)\,\mathbf{n}_0^f(s) + \kappa_g(s)\mathbf{n}_2^f(s)$ and the material strain vector $\kappa^f(s) = (\tau_g(s), 0, \kappa_g(s))$, with $\mathbf{n}_2^f(s)$ the binormal of the curve $\Gamma(s)$, and $\kappa_g(s)$ and $\tau_g(s)$ the geometric curvature and torsion, respectively.

Another popular material frame is the *Bishop frame*, which has the particularity to have a vanishing material twist. It has for Darboux vector $\mathbf{\Omega}^b(s) = \kappa_g(s)\mathbf{n}_2^f(s)$ and for material strain vector $\kappa^b(s) = (0, \kappa_1^b(s), \kappa_2^b(s))$ with $\kappa_1^b(s)$ and $\kappa_2^b(s)$ two functions satisfying $\left(\kappa_1^b(s)\right)^2 + \left(\kappa_2^b(s)\right)^2 = \kappa_g^2(s)$.

General case We see that there are multiple ways — actually an infinite number of ways — of framing Γ. It means that there are multiple framed curves that share the same underlying geometric curve.

Definition 1. *We say that two framed curves* $\mathcal{F}^a = \{\Gamma^a; \mathcal{R}^a\}$ *and* $\mathcal{F}^b = \{\Gamma^b; \mathcal{R}^b\}$ *are* equivalent *and we denote it by* $\mathcal{F}^a \equiv \mathcal{F}^b$ *when they share the same underlying geometric curve* $\Gamma^a = \Gamma^b$.

Note that since each framing is implicitly adapted (see discussion in Section 2.1), we necessarily have $\mathbf{n}_0^a = \mathbf{n}_0^b = \Gamma^{a'} = \Gamma^{b'}$ when the two framed curves

are equivalent. We are now interested to see how the equivalency condition translates to the corresponding material frame fields $\mathcal{R}^a$ and $\mathcal{R}^b$ and strain vector fields κ^a and κ^b, respectively.

3.2 Equivalent frame fields

Let $\mathbf{e_x}$ be the first canonical vector of $\mathbb{R}^3$, $\mathbf{e_x} = [1, 0, 0]^\top$. The following lemma establishes an equivalency relationship between the frames of equivalent framed curves.

Lemma 1. *Two framed curves* $\mathcal{F}^a = \{\Gamma^a(s); \mathcal{R}^a(s)\}$ *and* $\mathcal{F}^b = \{\Gamma^b(s); \mathcal{R}^b(s)\}$ *are equivalent if and only if*

$$\exists \theta \in \mathcal{C}^2_{([0,L],\mathbb{R})},\ \Gamma^a(0) = \Gamma^b(0) \quad \textit{and} \quad \forall s \in [0, L],\ \mathcal{R}^b(s) = \mathcal{R}^a(s)\,\mathcal{R}_\theta(s),$$

where $\mathcal{R}_\theta(s) = \begin{bmatrix} 1 & 0 & 0 \\ 0 & \cos\theta(s) & -\sin\theta(s) \\ 0 & \sin\theta(s) & \cos\theta(s) \end{bmatrix}$ *is the rotation of axis* $\mathbf{e_x}$ *and angle* $\theta(s)$.

Proof. Assume the existence of two framed curves $\mathcal{F}^a(s)$ and $\mathcal{F}^b(s)$ sharing the same geometric curve $\Gamma(s)$. Since both frames are orthonormal and adapted to Γ, one can be obtained from the other by a rotation of angle $\theta(s)$ around the tangent vector $\mathbf{n}_0(s)$. This relationship between $\mathcal{R}^a(s)$ and $\mathcal{R}^b(s)$ is illustrated in Figure 1(b), and mathematically reads $\mathcal{R}^b(s) = \mathcal{R}^a(s)\,\mathcal{R}_\theta(s)$, where $\mathcal{R}_\theta(s)$ represents the change of basis matrix from $\mathcal{R}^a(s)$ to $\mathcal{R}^b(s)$.

The other direction is proved by noticing that the two frames share the same tangent vector $\mathbf{n}_0(s)$ and thus have the same underlying geometric curve. □

3.3 Equivalent strain vector fields

The following theorem establishes the relationship between the strain vector fields of two equivalent framed curves.

Theorem 3.1. *Two framed curves* $\mathcal{F}^a = \{\Gamma^a(s); \mathcal{R}^a(s)\}$ *and* $\mathcal{F}^b = \{\Gamma^b(s); \mathcal{R}^b(s)\}$ *are equivalent if and only if*

$$\begin{cases} \Gamma^a_0 = \Gamma^b_0 & \text{(9a)} \\ \exists \theta_0 \in \mathbb{R},\ \mathcal{R}^a_0 = \mathcal{R}^b_0 \mathcal{R}_{\theta_0} & \text{(9b)} \\ \exists \theta \in \mathcal{C}^2_{([0,L],\mathbb{R})},\ \theta(0) = \theta_0 \textit{ and} & \text{(9c)} \\ \forall s \in [0, L],\ \kappa^b(s) = \mathcal{R}_{-\theta(s)} \left(\kappa^a(s) + \theta'(s)\mathbf{e_x}\right). & \text{(9d)} \end{cases}$$

Proof. First, we assume that $\mathcal{F}^a$ and $\mathcal{F}^b$ have the same underlying curve, i.e., $\Gamma^a = \Gamma^b = \Gamma$. By Lemma 1, there exists a scalar function θ such that $\theta(0) = \theta_0$ and

$$\forall s \in [0, L],\ \mathcal{R}^b(s) = \mathcal{R}^a(s)\mathcal{R}_{\theta(s)}.$$

On the one hand, using the Darboux equation (4) yields

$$\mathcal{R}^{b'} = \mathcal{R}^b[\kappa^b]_\times$$

and on the other hand, we have

$$\begin{aligned}
\mathcal{R}^{b'} &= (\mathcal{R}^a\mathcal{R}_\theta)' = \mathcal{R}^{a'}\mathcal{R}_\theta + \mathcal{R}^a\mathcal{R}'_\theta \\
&= \mathcal{R}^a[\kappa^a]_\times\mathcal{R}_\theta + \mathcal{R}^a[\theta'\mathbf{e_x}]_\times\mathcal{R}_\theta \quad \text{using (4) and decomposing } \mathcal{R}'_\theta \\
&= \mathcal{R}^a[\kappa^a + \theta'\mathbf{e_x}]_\times\mathcal{R}_\theta \\
&= \mathcal{R}^a\mathcal{R}_\theta[\mathcal{R}_{-\theta}(\kappa^a + \theta'\mathbf{e_x})]_\times \quad \text{using Equation (3) on rotations} \\
&= \mathcal{R}^b[\mathcal{R}_{-\theta}(\kappa^a + \theta'\mathbf{e_x})]_\times,
\end{aligned}$$

from which we deduce

$$\forall s \in [0, L],\ \kappa^b(s) = \mathcal{R}_{-\theta(s)}\left(\kappa^a(s) + \theta'(s)\mathbf{e_x}\right).$$

Second, we assume that Equation (9d) holds. We have

$$\begin{aligned}
(\mathcal{R}^a\mathcal{R}_\theta)' &= \mathcal{R}^{a'}\mathcal{R}_\theta + \mathcal{R}^a\mathcal{R}'_\theta \\
&= \mathcal{R}^a[\kappa^a]_\times\mathcal{R}_\theta + \mathcal{R}^a[\theta'\mathbf{e_x}]_\times\mathcal{R}_\theta \quad \text{using (4) and decomposing } \mathcal{R}'_\theta \\
&= \mathcal{R}^a[\kappa^a + \theta'\mathbf{e_x}]_\times\mathcal{R}_\theta \\
&= \mathcal{R}^a[\mathcal{R}_\theta\kappa^b]_\times\mathcal{R}_\theta \\
&= \mathcal{R}^a\mathcal{R}_\theta[\kappa^b]_\times \quad \text{using (3).}
\end{aligned}$$

Then by Cauchy's theorem, we obtain $\mathcal{R}_a\mathcal{R}_\theta = \mathcal{R}_b$, and using Lemma 1, $\Gamma_a = \Gamma_b$.

□

Special cases Let us derive Equation (9d) in the case when $\mathcal{R}^a$ is a special frame field (Frenet or Bishop), and $\mathcal{R}^b = \mathcal{R}$ is any material frame field adapted to Γ, characterized by the strain vector field $\kappa = (\kappa_0, \kappa_1, \kappa_2)$.

When $\mathcal{R}^a$ is the Frenet frame, we obtain

$$\begin{cases}
\kappa_0(s) = \tau_g(s) + \theta'(s) \\
\kappa_1(s) = \sin\theta(s)\,\kappa_g(s) \\
\kappa_2(s) = \cos\theta(s)\,\kappa_g(s),
\end{cases}$$

which is consistent with the relationships already provided in [37, Section 253].

When $\mathcal{R}^a$ is the Bishop frame, System (9d) boils down to

$$\begin{cases}
\kappa_0(s) = \theta'(s) \\
\kappa_1(s) = \cos\theta(s)\,\kappa_1^b(s) + \sin\theta(s)\,\kappa_2^b(s) \\
\kappa_2(s) = -\sin\theta(s)\,\kappa_1^b(s) + \cos\theta(s)\,\kappa_2^b(s).
\end{cases}$$

In particular, we retrieve the fact that the material twist $\kappa_0(s)$ of the material frame $\mathcal{R}(s)$ is given by the derivative of the angle $\theta(s)$. This nice property made the curve-angle (Γ, θ) parametrization of a material rod from the Bishop frame

particularly appealing [38] and is now preferred by many authors to the classical Euler angles parametrization. This reduced curve-angle parametrization was in particular leveraged in Computer Graphics for designing the so-called *discrete elastic rod* model, for which primary variables are discrete node positions of the centerline [16].

4 The inverse static design problem for a Kirchhoff rod

From the input curve $\Gamma(s)$, we aim at finding conditions on $\bar{\kappa}(s)$ and $\mathcal{R}(s)$ so that $\Gamma(s)$ coincides with the centerline of a Kirchhoff rod *at equilibrium* under gravity, framed by $\mathcal{R}(s)$.

4.1 Mapping between actual and natural framed curves

Starting from the static Kirchhoff equations, we obtain the following property, which, to the best of our knowledge, has not been formulated before,

Property 1. *For any framed curve $\{\Gamma_0; \mathcal{R}_0; \kappa(s)\}$ with the curve Γ as a centerline, Kirchhoff's equilibrium equations are satisfied if and only if $\bar{\kappa}(s)$ is solution to the explicit linear ODE of first order,*

$$\hat{\kappa}'(s) + \mathbb{K}_3^{-1} \left[\kappa(s)\right]_\times \mathbb{K}_3 \, \hat{\kappa}(s) = \mathbb{K}_3^{-1} \left[\mathbf{e_x}\right]_\times \mathcal{R}^\top(s) \mathbf{T}(s), \tag{10}$$

where $\hat{\kappa} = \bar{\kappa} - \kappa$ and the tension $\mathbf{T}(s)$ satisfies the linear momentum equation (6a) at equilibrium,

$$\mathbf{T}'(s) - \mathbf{p}(s) = 0, \quad \textit{i.e.,} \quad \mathbf{T}(s) = -\int_s^L \mathbf{p}(s).$$

In the special case of gravity, we have

$$\mathbf{T}'(s) - \rho S g \mathbf{e_z} = 0, \quad \textit{i.e.,} \quad \mathbf{T}(s) = -\int_s^L \rho S g \mathbf{e_z} = \rho S g (s - L)\, \mathbf{e_z}.$$

Moreover, we have the boundary condition $\bar{\kappa}(L) = \kappa(L)$, which reads

$$\hat{\kappa}(L) = 0. \tag{11}$$

Proof. Equation (10) can be simply derived from the angular momentum equation (6b) by first differentiating (7) and left-factorizing it by $\mathcal{R}(s)$ thanks to the Darboux equation (4), then rearranging the term $\mathbf{n}_0(s) \times \mathbf{T}(s)$ as $\mathcal{R}(s) \left(\mathbf{e_x} \times \mathcal{R}^\top \mathbf{T}(s)\right)$ using the property on rotation matrices (3), and finally multiplying the angular momentum equation by $\mathbb{K}_3^{-1} \mathcal{R}(s)^\top$. The boundary condition (11) directly stems from (8d). □

Equations (10) and (11) form a Cauchy problem, which admits a unique solution. Thus, to any framed curve $\mathcal{F} = \{\Gamma; \mathcal{R}\} = \{\Gamma_0; \mathcal{R}_0; \kappa(s)\}$, we can associate a unique natural framed curve $\bar{\mathcal{F}} = \{\bar{\Gamma}; \bar{\mathcal{R}}\} = \{\Gamma_0; \mathcal{R}_0; \bar{\kappa}(s)\}$ where $\bar{\kappa}$ is the unique solution to the Cauchy problem (10 – 11). In the following we prove that $\bar{\Gamma}$ is actually unique whatever the framing $\mathcal{R}$ chosen for the input curve Γ. The key is to show that all the $\bar{\kappa}$ solution to Cauchy problems with varying $\mathcal{R}$ are actually equivalent.

4.2 Equivalent natural strains

It is now time to enunciate our central theorem, which establishes the relation between natural framed curves that are associated to equivalent framed curves. We focus on the case where $\mathbf{T}(s)$ is independent of the framing of the curve. It is the case when the rod is only subjected to gravity for example.

Theorem 4.1. *The natural framed curves associated to two equivalent framed curves are equivalent, i.e.,*

$$\mathcal{F}^a \equiv \mathcal{F}^b \Longrightarrow \bar{\mathcal{F}}^a \equiv \bar{\mathcal{F}}^b.$$

Proof. To prove this result, we use an equivalent formulation of Equation (10), corresponding to its scaling by $\mathcal{R}\,\mathbb{K}_3$,

$$\mathcal{R}\,\mathbb{K}_3\,\hat{\kappa}' + \mathcal{R}\,[\kappa]_\times\,\mathbb{K}_3\,\hat{\kappa} = \mathbf{n}_0 \times \mathbf{T}(s) \quad \text{with } \hat{\kappa} = \bar{\kappa} - \kappa. \tag{12}$$

We assume that we have two equivalent framings $\mathcal{R}^a$ and $\mathcal{R}^b$ for the input curve Γ, so that, according to Lemma 1 and Theorem 3.1,

$$\mathcal{R}^b = \mathcal{R}^a\,\mathcal{R}_\theta \quad \text{and} \quad \kappa^b = \mathcal{R}_{-\theta}\,(\kappa^a + \theta'\mathbf{e_x})\,. \tag{13}$$

We also suppose that $\bar{\kappa}^a$ is solution of Equation (12) for $\mathcal{R} = \mathcal{R}^a$ and $\kappa = \kappa^a$, that is

$$\mathcal{R}^a\,\mathbb{K}_3\,\hat{\kappa}^{a'} + \mathcal{R}^a\,[\kappa^a]_\times\,\mathbb{K}_3\,\hat{\kappa}^a = \mathbf{n}_0 \times \mathbf{T}(s). \tag{14}$$

We show in the following that $\bar{\kappa}^b = \mathcal{R}_{-\theta}\,(\bar{\kappa}^a + \theta'\mathbf{e_x})$, which is equivalent to $\bar{\kappa}^a$ (with the particular angular function θ), is solution of Equation (12) for $\mathcal{R} = \mathcal{R}^b$ and $\kappa = \kappa^b$.

We start by noticing that

$$\begin{aligned}
\hat{\kappa}^b &= \bar{\kappa}^b - \kappa^b \\
&= \mathcal{R}_{-\theta}\,(\bar{\kappa}^a + \theta'\mathbf{e_x}) - \mathcal{R}_{-\theta}\,(\kappa^a + \theta'\mathbf{e_x}) \text{ using the definition of } \bar{\kappa}^b \text{ and (13)} \\
&= \mathcal{R}_{-\theta}\,(\bar{\kappa}^a - \kappa^a) \\
&= \mathcal{R}_{-\theta}\,\hat{\kappa}^a,
\end{aligned} \tag{15}$$

and that

$$\begin{aligned}
\hat{\kappa}^{b'} &= (\mathcal{R}_{-\theta}\,\hat{\kappa}^a)' \text{ using (15)} \\
&= (\mathcal{R}_{-\theta})'\,\hat{\kappa}^a + \mathcal{R}_{-\theta}\,\hat{\kappa}^{a'} \\
&= -\theta'\,[\mathbf{e_x}]_\times\,\mathcal{R}_{-\theta}\,\hat{\kappa}^a + \mathcal{R}_{-\theta}\,\hat{\kappa}^{a'}.
\end{aligned} \tag{16}$$

Then, since we are considering the isotropic case (isotropic material and circular cross-section), we have $\mathcal{K}_1 = \mathcal{K}_2$, and one key consequence is that the diagonal matrix $\mathbb{K}_3$ commutes with any 3D matrix A of the form $A = \mathrm{diag}_3(a, B)$ where a is a scalar and B a 2D matrix. In particular, we have

$$\mathcal{R}_\theta \, \mathbb{K}_3 = \mathbb{K}_3 \, \mathcal{R}_\theta \quad \text{and} \quad \mathbf{e_x} \, \mathbb{K}_3 = \mathbb{K}_3 \, \mathbf{e_x}. \tag{17}$$

We now derive the left-hand side of Equation (12) for $\mathcal{R} = \mathcal{R}^b$ and $\kappa = \kappa^b$, by replacing $\mathbb{R}^b$, κ^b, $\hat{\kappa}^b$, and $\hat{\kappa}^{b'}$ with their expressions given by (13), (15), and (16), respectively. This yields

$$\begin{aligned}
&\mathcal{R}^b \, \mathbb{K}_3 \, \hat{\kappa}^{b'} + \mathcal{R}^b \, \left[\kappa^b\right]_\times \, \mathbb{K}_3 \, \hat{\kappa}^b \\
&\quad = \mathcal{R}^a \, \mathcal{R}_\theta \, \mathbb{K}_3 \, \left(-\theta' \, \left[\mathbf{e_x}\right]_\times \, \mathcal{R}_{-\theta} \, \hat{\kappa}^a + \mathcal{R}_{-\theta} \, \hat{\kappa}^{a'}\right) + \mathcal{R}^a \, \mathcal{R}_\theta \, \left[\mathcal{R}_{-\theta} \, (\kappa^a + \theta' \mathbf{e_x})\right]_\times \, \mathbb{K}_3 \, \mathcal{R}_{-\theta} \, \hat{\kappa}^a \\
&\quad = \mathcal{R}^a \, \mathbb{K}_3 \, \left(-\theta' \, \left[\mathbf{e_x}\right]_\times \, \hat{\kappa}^a + \hat{\kappa}^{a'}\right) + \mathcal{R}^a \, \mathcal{R}_\theta \, \left[\mathcal{R}_{-\theta} \, (\kappa^a + \theta' \mathbf{e_x})\right]_\times \, \mathcal{R}_{-\theta} \, \mathbb{K}_3 \, \hat{\kappa}^a \quad \text{using (17)} \\
&\quad = \mathcal{R}^a \, \mathbb{K}_3 \, \left(-\theta' \, \left[\mathbf{e_x}\right]_\times \, \hat{\kappa}^a + \hat{\kappa}^{a'}\right) + \mathcal{R}^a \, \left[\kappa^a + \theta' \mathbf{e_x}\right]_\times \, \mathbb{K}_3 \, \hat{\kappa}^a \quad \text{using (3)} \\
&\quad = \mathcal{R}^a \, \mathbb{K}_3 \, \hat{\kappa}^{a'} + \mathcal{R}^a \, \left(-\theta' \, \left[\mathbf{e_x}\right]_\times + \left[\kappa^a + \theta' \mathbf{e_x}\right]_\times\right) \, \mathbb{K}_3 \, \hat{\kappa}^a \quad \text{factorizing and using (17)} \\
&\quad = \mathcal{R}^a \, \mathbb{K}_3 \, \hat{\kappa}^{a'} + \mathcal{R}^a \, \left[\kappa^a\right]_\times \, \mathbb{K}_3 \, \hat{\kappa}^a \\
&\quad = \mathbf{n}_0 \times \mathbf{T}(s) \quad \text{using (14)}.
\end{aligned}$$

□

From the above proof, we remark that when two input frames differ from an angular function $\theta(s)$, then the two associated natural frames also differ from the same angular function $\theta(s)$.

Uniqueness of the natural configuration immediately follows from Theorem 4.1,

Corollary 4.1. *The natural configuration $\bar{\Gamma}$ is independent of the framing of the input curve Γ. It is thus unique.*

As a consequence, combining Property 1 and Corollary 4.1 provides us with a simple inversion procedure, described in Section 4.3. As a side note, we would like to mention that while the natural configuration $\bar{\Gamma}$ of a Kirchhoff rod matching a given curve Γ at equilibrium is unique, the reverse is not true. Indeed, different rod equilibria may correspond to the same natural configuration (imagine for instance a 2D cantilever beam bent either on the right or on the left). Inverting each one of such different equilibria would of course lead to the exact same natural configuration. This brings an interesting view on the *well-posedness* of the static Kirchhoff problem: while the direct problem is ill-posed (multiplicity of solutions due to the presence of bifurcations), the inverse problem is actually well-posed in the Hadamard sense. We have indeed proved here that the solution to the inverse problem exists and is unique. Continuity w.r.t. data is straightforward due to the fact that Equation (10) is linear in $\bar{\kappa}$. Some hints at the sensitivity of the inversion process are in turn given in Section 55.3.

4.3 Inversion procedure

Given an arbitrary curve Γ, we may first frame it by choosing *any* adapted material frame field (for instance the Frenet frame), then compute the unique solution $\bar{\kappa}$ to the Cauchy problem (10–11), and finally integrate the full Darboux problem (5) for computing first the natural frame field $\bar{\mathcal{R}}$ and finally the unique natural shape $\bar{\Gamma}$. Note that changing the initial framing may of course change the value of the resulting natural strain vector field $\bar{\kappa}$ and of the natural frame field $\bar{\mathcal{R}}$, but *not* the value of the natural configuration $\bar{\Gamma}$. Section 5 gives some numerical examples illustrating this inversion procedure.

5 Numerical results

The goal of our inversion procedure is to find the unique natural shape $\bar{\Gamma}$ for a given equilibrium state Γ. To numerically solve this problem we need to retrieve, as a preliminary step, an equilibrium configuration $\{\mathcal{R}; \kappa\}$ corresponding to a given equilibrium shape Γ. In this work equilibrium configurations are obtained by two means. One is by defining the equilibrium shape Γ as a model shape for which a configuration $\{\mathcal{R}; \kappa\}$ is analytically accessible by solving the Frenet-Serret Equations. The other is by using a static simulator to find synthetic equilibria achieved from an initial rest shape; in this case the outputs of the used simulator are the shape $\Gamma(s)$ and the strain field $\kappa(s)$, however by solving Darboux's equations (see eq 4) we can compute the corresponding frame field.

Numerical scheme Once we have an equilibrium configuration, our numeric solution consists in three steps. First we solve for $\bar{\kappa}$ in Equations (10–11), which is an initial valued problem consisting of 3 coupled equations for the components of the strain field $\hat{\kappa}(s) = \bar{\kappa}(s) - \kappa(s)$, and if expanded, reads as follows,

$$\begin{cases} \mathcal{K}_0\hat{\kappa}_0'(s) = \mathcal{K}_2\kappa_1(s)\hat{\kappa}_2(s) - \mathcal{K}_1\kappa_2(s)\hat{\kappa}_1(s) \\ \mathcal{K}_1\hat{\kappa}_1'(s) = \mathcal{K}_0\kappa_2(s)\hat{\kappa}_0(s) - \mathcal{K}_2\kappa_0(s)\hat{\kappa}_2(s) - \pi a^2\rho g(s-L)b_2 \\ \mathcal{K}_2\hat{\kappa}_2'(s) = \mathcal{K}_1\kappa_0(s)\hat{\kappa}_1(s) - \mathcal{K}_0\kappa_1(s)\hat{\kappa}_0(s) + \pi a^2\rho g(s-L)n_2, \end{cases} \tag{18}$$

subjected to the condition, $\bar{\kappa}(L) = \kappa(L)$ equivalent to $\hat{\kappa}(L) = 0$, and where $(\mathcal{K}_0, \mathcal{K}_1, \mathcal{K}_2)$ is the trace of the stiffness matrix $\mathbb{K}_3$, and b_2 and n_2 are the z-components of the binormal and normal vectors respectively, in the frame $\mathcal{R}$. To deal with this system of coupled equations we implement a standard numerical solver in MATLAB, relying on the builtin function ode45, which deals by itself with the condition at the end of the rod $\hat{\kappa}(L) = 0$. Once we obtain a solution for $\hat{\kappa}$, we straighforwardly compute $\bar{\kappa}(s) = \hat{\kappa}(s) + \kappa(s)$.

The next step is to solve Darboux's equations (see eq 4), which correspond to solve 3 systems of 3 coupled equations each, with the enforced clamped frame condition $\bar{\mathcal{R}}(0) = \mathcal{R}(0)$. Again ode45 in MATLAB solves this 3 systems separately, and outputs the frame for the rest shape, $\bar{\mathcal{R}}$.

On the final step we retrieve the rest shape by integrating the tangent, equivalent to solve $\bar{\Gamma}'(s) = \hat{t}(s)$, which is a simple integration of 3 uncoupled first degree differential equations with the initial value $\Gamma(0) = \bar{\Gamma}(0)$.

Numerical experiments In the following we illustrate our theoretical results through three kinds of numerical experiments. First we apply our inversion procedure to three arbitrary model cases with analytically known equilibrium configurations, but whose natural shapes are unknown (Section 5.1). Then we show that our inversion procedure provides, as predicted by Corollary 4.1, the same natural shape whatever the chosen input frame (Section 5.2). Finally we examine the sensitivity of our inversion procedure w.r.t. input data by applying our algorithm to initially horizontal straight rods with different Elastic moduli (Section 5.3).

5.1 Application to the inversion of model curves

In this section we tackle the case of arbitrary curves which are freely chosen by the user. In particular, we consider the three following model space curves of different lengths that we parameterize by the function of the arc length $t(s)$,

- **Helix:** $\Gamma_h(s) = [R\cos(t(s)), R\sin(t(s)), -\lambda t(s)]$, for $s \in [0, L_h]$ with $L_h = 0.3(\mathrm{m})$,
- **Conical helix:** $\Gamma_c(s) = [Ae^{t(s)/\omega}\cos(\omega t(s)), Ae^{t(s)/\omega}\sin(\omega t(s)), -\lambda t(s)]$, for $s \in [0, L_c]$ with $L_c = 0.23(\mathrm{m})$,
- **X-Z Planar wave:** $\Gamma_w(s) = [A\sin(\omega t(s)), 0, -\lambda t(s)]$, for $s \in [0, L_w]$ with $L_w = 0.7(\mathrm{m})$.

These three shapes are illustrated in Figure 2 (black dashed lines). Our goal is now to interpret these shapes as the equilibrium configurations of Kirchhoff rods. Note that since these shape are analytically defined, the configuration $\{\mathcal{R}; \kappa\}$ is analytically accessible by using the Frenet-Serret equations.

We set material parameters in the range of very soft materials. We choose for the **Helix** $E_h = 5$ MPa, for the **Conical helix** $E_c = 3.5$ MPa and for the **X-Z Planar wave** $E_w = 23$ MPa. Remaining parameters are set, for all curves, as follows: gravity $g = 9.8\mathrm{m/s}^2$, volumetric mass density $\rho = 1200\mathrm{kg/m}^3$, Poisson ratio $\nu = 0.5$, and cross-sectional radius $a = 1.5\mathrm{mm}$.

As we mention before for each of theses curves the corresponding Frenet frame $\mathcal{R}^f(s)$ is analytically accessible. Similarly, we can compute the geometric curvature $\kappa_g(s)$ and torsion $\tau_g(s)$ in an exact manner, through 2-times and 3-times differentiation of the model curve, respectively. To compute $\bar{\Gamma}_h$, $\bar{\Gamma}_c$, and $\bar{\Gamma}_w$, we run the inversion procedure described at the beginning of this section.

Figure 2 depicts, for each model curve, both the input shape (black dashed lines), and the corresponding natural shape computed by our procedure (light grey rod). While our input shapes are elementary and the mechanical parameters used very close to that of real objects, the retrieved natural shapes are

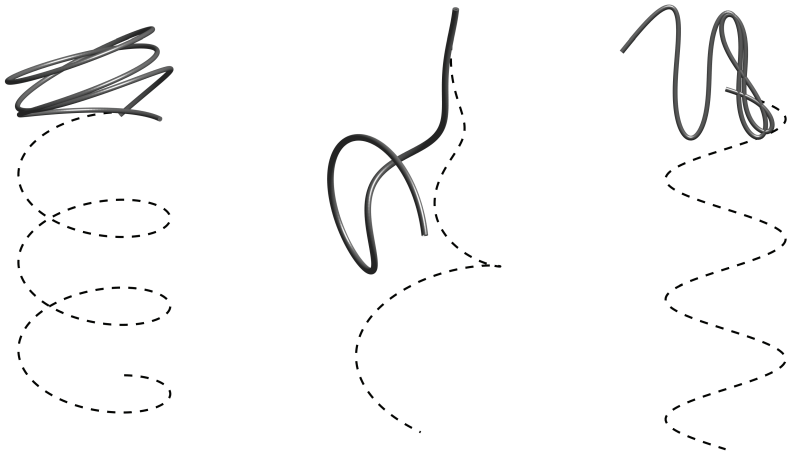

Figure 2: Model space curves (dashed black lines) and their corresponding natural shapes (light grey rod). From left to right, **Helix** with radius $R = 15\text{mm}$ and pitch $2\pi\lambda$ with $\lambda = -3.18\text{mm}$; **Conical helix** with pseudo-amplitude $A = 0.8\text{mm}$, pseudo-wavenumber $\omega = 2\text{m}^{-1}$ and pseudo-wavelength $\lambda \sim 16\text{mm}$; and **X-Z Planar wave** with amplitude $A = 50\text{mm}$, and wavenumber $\omega \sim 63\text{m}^{-1}$.

rather complex: it would be impossible to "guess" them without using an inverse design procedure.

To help visualize the practical interest of our results, we have simulated the direct dynamics of each retrieved rod, using a dynamic implementation of the super-helix model [15], with 200 rod elements. The simulator is initialized at time $t = 0$ with the natural shape as the actual configuration, and zero velocity; then gravity is applied together with some damping, and the simulator computes the new configuration of the rod at each next time step. For each case, we observe that the rod dynamics converges to the (dashed) input shape, showing that the latter corresponds to an equilibrium configuration. These three simulations are included in our supplementary video. Note that to achieve such results and, in particular, guarantee that the input shape is not only an equilibrium, but a *stable* equilibrium, we had to choose the bending modulus EI and the linear mass density ρS in a proper range of values (the rod should not be too soft nor too heavy), similarly to what was predicted in the discrete case [33]. In the future we plan to establish the exact stability conditions in the continuous case.

Finally, it is noteworthy that in the **X-Z Planar wave** example, the retrieved natural configuration is also planar. Indeed, looking at the ODE (18), it is easy to prove that when the input shape Γ is planar and when the external force (gravity) is lying in the same plane, then the natural configuration $\bar{\Gamma}$ is necessarily planar. We leave the proof as an exercice to the interested reader.

5.2 Illustration of the frame invariance

In the previous section we have always used the Frenet frame to frame our input curves. However, Corollary 4.1 guarantees that the natural shape is independent of the initial framing. To illustrate this invariance result, we consider the **Helix** curve from Section 5.1, and frame it in different ways. From its Frenet frame $\mathcal{R}^f$ we can compute the Bishop frame $\mathcal{R}^b$, which is equivalent to finding the rotation defined by the function $\theta(s)$ about the tangent, such that the first coordinate of the strain vector field vanishes. For the **Helix** case, this function is $\theta^b(s) = -\lambda s/(R^2 + \lambda^2)$, where R and λ are set to be 15mm and -3.18mm repectively, similarly to previous section (see Figure 2). Alongside, we present two other arbitrary frames F^{lin} and F^{exp}, obtained by rotating the Frenet frame around the tangent by the functions $\theta^{\text{lin}}(s) = -6\pi s/L$ and $\theta^{\text{exp}}(s) = -8\pi e^{s/L}$, respectively.

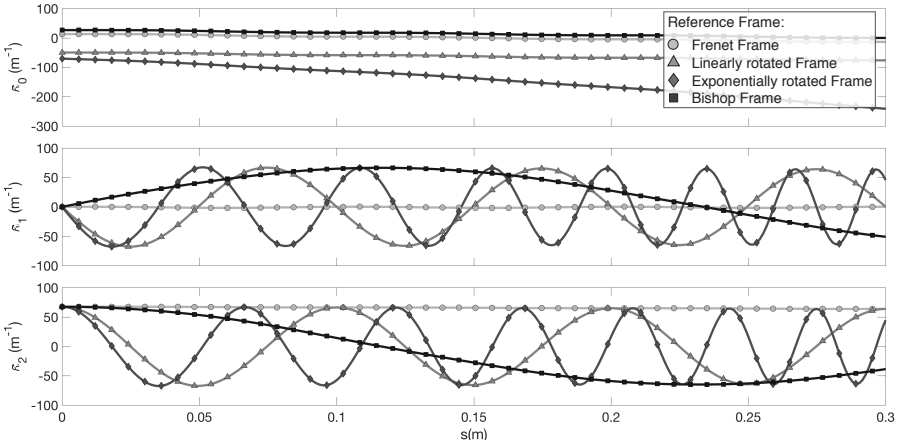

Figure 3: Resulting natural strain vector field for the same input curve **Helix**, framed in different ways. From top to bottom we show each component of the natural strain vector field $\bar{\kappa}$.

The procedure to invert the **Helix** shape using these different frames is still the same as before. We compute the frames $\mathcal{R}^b$, $\mathcal{R}^{\text{lin}}$, and $\mathcal{R}^{\text{exp}}$, and the corresponding strain vector fields κ^b, κ^{lin}, and κ^{exp}. With these values we feed our ODE solver to resolve (18), and obtain $\bar{\kappa}^b$, $\bar{\kappa}^{\text{lin}}$, and $\bar{\kappa}^{\text{exp}}$. These new solutions are represented in Figure 3 and compared against our previous solution $\bar{\kappa}^f$ obtained for the Frenet frame.

We note that depending on the chosen framing of the input curve, the resulting values of the natural strain vectors are notably dissimilar. This is due to the fact that we are projecting the strains in frames that are very different, as exemplified for the Frenet and Bishop frame in Figure 4 (left and middle panels respectively). Despite this strong mismatch between values of $\bar{\kappa}$, after solving the Darboux problem (5), we obtain the same identical curve $\bar{\Gamma}$ for all cases, see

Figure 4 right panel.

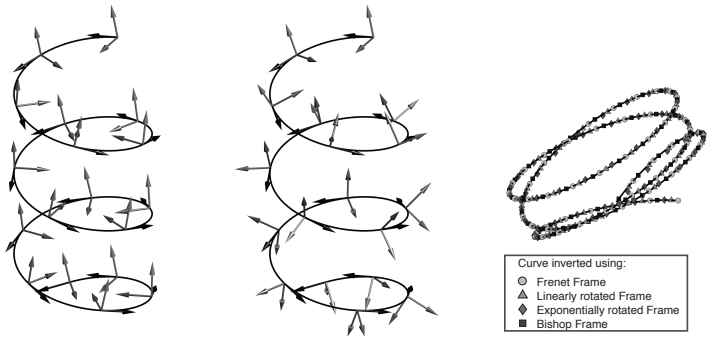

Figure 4: **Left panel**, Sampling of the Frenet frame and, **middle panel**, the Bishop frame. **Right panel**, reconstructed natural shapes using the four frames.

5.3 Cantilever beam and sensitivity to input data

Using a static implementation of the super-helix model [15] based on an optimal control formulation [39], we have run simulations of initially straight horizontal rods deformed by the action of gravity. For these simulations we have set the cross-sectional radius to $a = 2.225$ mm, the length of the rods to $L = 0.2$ m, the volumetric mass density to $\rho = 1200$ kg/m^3, and the Poisson ratio $\nu = 0.5$, and we vary the elastic modulus within the range $10^5 - 10^9$ Pa. The simulator gives us the equilibrium strain field from which we can compute the corresponding frame by solving Darboux's equations, hence we obtain for each Elastic modulus value an equilibrium configuration, $\{\mathcal{R}; \kappa\}$.

The resulting equilibrium shapes, see bottom panel in Figure 5, show a wide range of deformation. On the top panel in Figure 5, it is clear that our procedure returns perfectly horizontal rest shapes for high values of the Elastic moduli. However, as the deformation increases, our solution begins to deviate.

To properly compare our experiments with general cases, we use the natural length scale of the problem known as the Gravito-Bending length, and defined as $L_{gb} = (r^2 E/4\rho g)^{1/3}$ in [5], which compares the amount of gravitational work required to bend a rod with given mechanical and geometrical characteristics. To quantify the deviation of the rod from the horizontal perfect solution, we chose the most critical value, namely $max(z(s))$. From the inset in Figure 5 it is noticeable that the error decreases very quickly, only the error for the two most deflected rod is above 1% of the rod length. To give some context regarding real objects, a 15 cm human hair with a radius of 50μm will have a value of $L_{gb}/L = 0.24$, sufficient enough for this procedure to give a result with less than 1% error.

In order to understand where this deviation comes from, we have first generated equilibrium solutions with low number of elements (~ 200) and then we

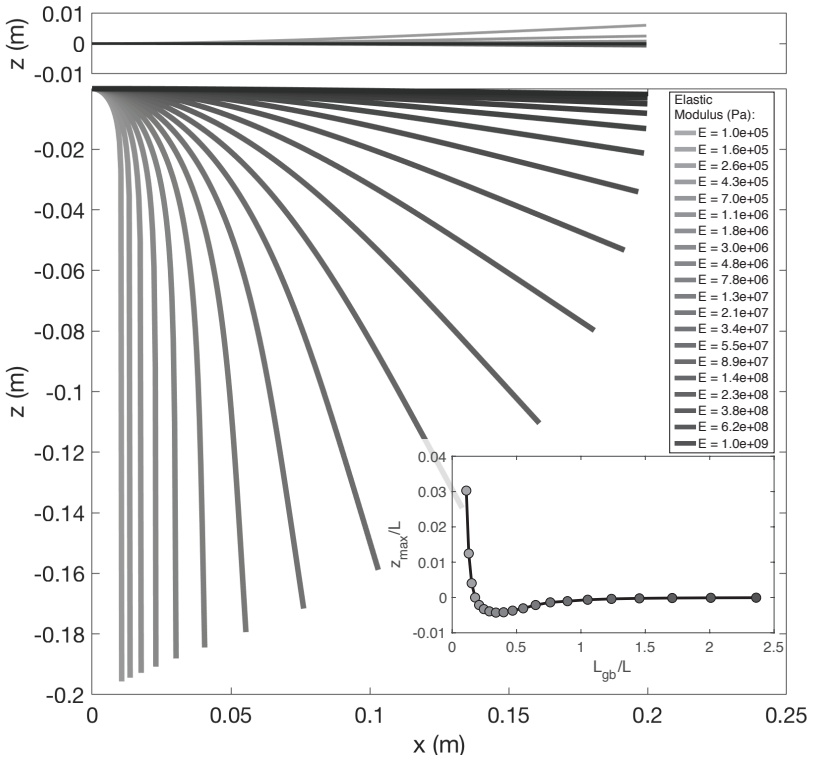

Figure 5: On the top panel we show the rest shapes obtained from our inversion procedure using as input the equilibrium shapes display on the bottom panel. The inset shows the $max(z(s))$ as a function gravito-bending length normalised by the rod length.

have progressively refined them. During refinement, we have observed that the inversion error becomes asymptotically smaller. The data we are presented in Figure 5 correspond to very high resolution simulations, consisting of 50,000 elements. This indicates that the source of error comes from imprecisions of input data, which, in the case of highly deformed rods, are exacerbated due to a very high sensitivity of our inversion process w.r.t. input data. We plan to work on this sensitivity issue in the future (see Section 6).

6 Discussion

Limitations To achieve our uniqueness result, we have made several important assumptions. First, we have restricted our study to the Kirchhoff thin elastic rod model, which is perfectly inextensible and unshearable. Considering a more general model such as a Timoshenko beam would imply adding stretch-

ing and shearing energies to the model. Shearing energy is only meaningful for thick fibers, a case that we disregard here. Now if we consider a finite streching energy, it may be combined to a finite bending energy in different proportions so that in the end, both compensate each other and yield the same equilibrium shape. We thus strongly suspect that allowing the rod to stretch significantly will break our uniqueness result. We are currently working on proving this result. That said, we note that the Kirchhoff rod model is sufficient to capture accurately the deformation of real elastic fibers in a fixed-free boundary conditions setup, since in this case stretching is negligible compared to bending. In our view, focusing on this model is thus not restrictive, even in the perspective of other clamping scenarios we plan to study, in which bending actually always predominates over stretching.

Second, we have supposed the rod to be isotropic, from both a material and geometrical viewpoint ($\mathcal{K}_1 = \mathcal{K}_2$). If this assumption does not hold, then the proof of Theorem 4.1 breaks. Indeed, isotropy yields commutativity of the stiffness matrix $\mathbb{K}_3$ with any 3×3 matrix with a left-top diagonal term, a key property for proving the equivalence of natural framed curves associated to equivalent framed curves. In the anisotropic case, uniqueness of the natural configuration is thus not guaranteed anymore, as illustrated in Figure 6 where we have applied our inversion algorithm to a rod with an ellipical cross-section, using different input framings. This result is actually rather intuitive: for an anisotropic rod like a thin ribbon, the sole knowledge of the centerline is not enough to determine the natural configuration; the entire cross-sectional field, that is the way the cross-section is oriented along the centerline, is needed to remove ambiguities. If in contrast one possesses the full geometry of the rod, that is the centerline plus the cross-sectional field, then one may reconstruct the material frame field (for instance by identifying the evolution of the principal axes of the cross-section), hence the material curvature field, and then retrieve the unique natural curvature field yielding a unique natural shape.

Third, we have only considered gravity as an external force field, but our theoretical framework remains valid for other force fields provided these are unequivocally defined and frame-invariant (that is, independent of θ and thus of κ and $\bar{\kappa}$). For instance adding a known punctual contact force, or an electrostatic force, would fit in with our framework. However, typical force fields which do not satisfy the request above are dry frictional forces, since they are indeterminate: they should belong to the Coulomb friction cone, but their magnitude and direction are not known. Similarly to what we have shown in the past in the discrete settings where the inverse problem has an infinity of solutions [40], in the continuous case the presence of Coulomb friction force also breaks our uniqueness result: to each different friction force satisfying the Coulomb conical constraint, it may correspond a different natural shape for the equilibrium to be satisfied.

Then, we have restricted the boundary conditions to the case where one end of the rod is clamped while the other is free. This scenario is valid for wide a range of naturally growing systems such as hair or plants. Many applications however involve different settings, especially fixed-fixed boundary conditions,

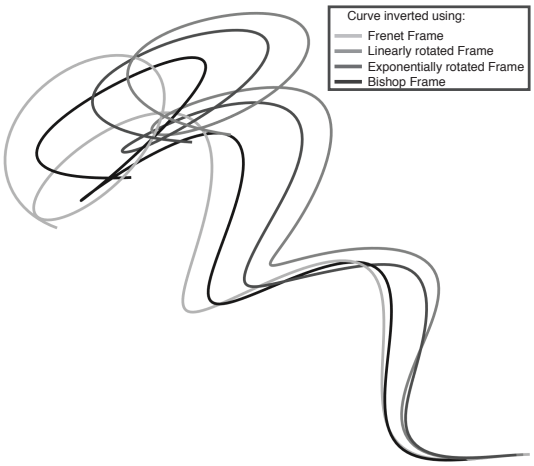

Figure 6: Inversion of the **Helix** curve with an elliptical cross-section, using four different input framings. Due to the anisotropy of the cross-section, our invariance result of the natural shape w.r.t. the framing is not valid anymore. This also means that in the anisotropic case, the sole data of the centerline is not sufficient to determine unequivocally the natural shape of the rod.

e.g., cables that are clamped at both ends. Without the proper knowledge of forces or torques applied at both ends, it is likely that the uniqueness result will break again, as in the frictional contact case. Imagine for instance a naturally straight rod and a naturally twisted rod. For them to yield the same equilibrium, it is sufficient to apply appropriate torques to the two fixed ends of the naturally straight rod. In the future we would like to study in deeper details how to disambiguate more general settings with non-straight rods subject to fixed-fixed boundary conditions.

Finally, we have only considered inverse statics in that paper, but a natural extension of our work would be to take dynamic data as input and to retrieve more information than a natural shape. When a Kirchhoff rod is under dynamic motion, Equation (10) still holds, the only difference being the expression of the tension T(s,t), which now incorporates at each time t the linear acceleration of the rod $\ddot{\Gamma}(s,t)$. If the acceleration field is entirely known for a certain time $t^\star$, then our results apply exactly as in the static case. If now accelerations are only partially known at different instants in time, our inverse procedure could be leveraged to recover missing acceleration data by using the property that all recovered natural shapes should be identical.

Future Work Overall, our uniqueness result along with a practical algorithm to recover the natural shape offer some promising developments and applications in the long run.

On the one hand, as we have already started to numerically investigate,

our inversion procedure could be used to *design* and automatically *fabricate* complex rod shapes that would match the user input in the presence of external forces. To make such a process feasible in practice, a number of theoretical and practical issues would need to be examined. First, as already pointed out in the result section, some conditions guaranteeing the stability of the input shape should be established to select appropriate material parameters. Then, unfeasible designs should be automatically avoided, such as self-interpenetrating natural shapes (like those in Figure 2, left and right) or material parameters that are out-of-range for fabrication.

On the other hand, our inversion procedure could be leveraged as a merely *non-invasive* identification pipeline, which would allow to recover physical parameters of a fiber solely from the observation of its shape under external forces. It could subsequently serve to control the exact amount of input information needed (e.g., a minimal number of poses) to allow for an accurate *identification* process, not only of the natural rod configuration, but also of its material parameters. The major challenge here stems from the accuracy of measurement of the input data. Indeed, our preliminary numerical tests (see Section 55.3) show that the solution to the ODE (10) is very sensitive to the input data κ. To add a supplementary difficulty, computing actual material strains κ requires the estimation of high-order derivatives of the input shape – for instance, for the Frenet frame, at least third-order derivatives. We are currently working on this issue, with the idea that a direct rod simulator could help estimate such high-order derivatives.

7 Conclusion

In this paper we have introduced the inverse static design problem for isotropic Kirchhoff rods, and have proved that the solution to this problem is unique, regardless of the infinite set of possible framings for the input curve.

For a few decades, several communities, from Computational Mechanics to Computer Graphics, have been interested in elastic inverse design problems. This growing interest has been especially boosted by the advent of additive fabrication, making it possible to fabricate models with predicted properties, and check for their validity in practice. In the case of nonlinear elastic fibers, our analysis reveals an exact and unique mapping from the deformed to the natural configuration. This allows for a straighforward inversion procedure, instead of "blindly" relying upon some nonlinear optimization algorithms as done in previous work. Such a new insight could be leveraged in the future for various applications such as the automatic design of rod-based systems at equilibrium, or the development of non-invasive parameter identification protocols.

8 Acknowledgements

We are grateful to Alejandro Blumentals and Eric Madaule for their help on software. We would also like to thank the investigators of the national Amiqual4Home project (ANR-11-EQPX-0002) for their help on the ongoing devel-

opment of the experimental side of our project. This work was supported by the European Research Council grant GEM (StG-2014-639139).

References

[1] Kirchhoff G. 1859 Ueber das Gleichgewicht und die Bewegung eines unendlich dünnen elastischen Stabes.. *Journal für die reine und angewandte Mathematik* **56**, 285–313.

[2] Dill E. 1992 Kirchhoff's theory of rods. *Archive for History of Exact Sciences* **44**, 1–23.

[3] Cosserat E, Cosserat F. 1909 *Théorie des corps déformables*. Hermann.

[4] Antman S. 1995 *Nonlinear Problems of Elasticity*. Springer Verlag.

[5] Audoly B, Pomeau Y. 2010 *Elasticity and Geometry: from hair curls to the nonlinear response of shells*. Oxford University Press.

[6] Furrer P, Manning R, Maddocks J. 2000 DNA rings with multiple energy minima. *Biophysical journal* **79**, 116–136.

[7] Neukirch S. 2004 Extracting DNA Twist Rigidity from Experimental Supercoiling Data. *Phys. Rev. Lett.* **93**, 198107.

[8] Benham C, Mielke S. 2005 DNA Mechanics. *Annual Review of Biomedical Engineering* **7**, 21–53.

[9] Goriely A, Tabor M. 1998 Spontaneous helix hand reversal and tendril perversion in climbing plants. *Physical Review Letters* **80**, 1564–1567.

[10] Goriely A, Neukirch S. 2006 Mechanics of Climbing and Attachment in Twining Plants. *Physical Review Letters* **97**, 184302.

[11] Yabuta T. 1984 Submarine cable kink analysis. *Bulletin of JSME* **27**, 1821–1828.

[12] Goyal S, Perkins NC, Lee CL. 2005 Nonlinear dynamics and loop formation in Kirchhoff rods with implications to the mechanics of DNA and cables. *Journal of Computational Physics* **209**, 371–389.

[13] Pai D. 2002 Strands: Interactive Simulation of Thin Solids using Cosserat Models. *Computer Graphics Forum (Proc. Eurographics'02)* **21**, 347–352.

[14] Chentanez N, Alterovitz R, Ritchie D, Cho L, Hauser KK, Goldberg K, Shewchuk JR, O'Brien JF. 2009 Interactive Simulation of Surgical Needle Insertion and Steering. *ACM Transactions on Graphics (Proc. ACM SIGGRAPH'09)* pp. 88:1–88:10.

[15] Bertails F, Audoly B, Cani MP, Querleux B, Leroy F, Lévêque JL. 2006 Super-Helices for Predicting the Dynamics of Natural Hair. *ACM Transactions on Graphics (Proc. ACM SIGGRAPH'06)* **25**, 1180–1187.

[16] Bergou M, Wardetzky M, Robinson S, Audoly B, Grinspun E. 2008 Discrete elastic rods. *ACM Transactions on Graphics (Proc. ACM SIGGRAPH'08)* **27**, 1–12.

[17] Champneys A, Van der Heijden G, Thompson J. 1997 Spatially complex localization after one-twist-per-wave equilibria in twisted circular rods with initial curvature. *Philosophical Transactions of the Royal Society of London. Series A: Mathematical, Physical and Engineering Sciences* **355**, 2151–2174.

[18] McMillen T, Goriely A. 2002 Tendril perversion in intrinsically curved rods. *Journal of Nonlinear Science* **12**, 241–281.

[19] Lazarus A, Miller JT, Metlitz M, Reis PM. 2013 Contorting a heavy and naturally curved elastic rod. *Soft Matter* **9**, 8274–8281.

[20] Miller J, Lazarus A, Audoly B, Reis P. 2014 Shapes of a Suspended Curly Hair. *Physical Review Letters* **112**, 068103.

[21] Jawed MK, Da F, Joo J, Grinspun E, Reis PM. 2014 Coiling of elastic rods on rigid substrates. *Proceedings of the National Academy of Sciences* **111**, 14663–14668.

[22] Beck J, Woodbury K. 1998 Inverse problems and parameter estimation: integration of measurements and analysis. *Measurement Science and Technology* **9**, 839.

[23] Turco E. 2017 Tools for the numerical solution of inverse problems in structural mechanics: review and research perspectives. *European Journal of Environmental and Civil Engineering* **21**, 509–554.

[24] Bonnet M, Constantinescu A. 2005 Inverse problems in elasticity. *Inverse problems* **21**, R1.

[25] Gladwell G. 1986 The inverse problem for the Euler-Bernoulli beam. In *Proceedings of the Royal Society of London A: Mathematical, Physical and Engineering Sciences* vol. 407 pp. 199–218. The Royal Society.

[26] Twigg CD, Kačić-Alesić Z. 2011 Optimization for Sag-free Simulations. In *Proceedings of the 2011 ACM SIGGRAPH/Eurographics Symposium on Computer Animation* SCA '11 pp. 225–236 Vancouver, Canada. ACM-EG.

[27] Fachinotti VD, Cardona A, Jetteur P. 2008 Finite element modelling of inverse design problems in large deformations anisotropic hyperelasticity. *International Journal for Numerical Methods in Engineering* **74**, 894–910.

[28] Albanesi AE, Fachinotti VD, Cardona A. 2010 Inverse finite element method for large-displacement beams. *International Journal for Numerical Methods in Engineering* **84**, 1166–1182.

[29] Chen X, Zheng C, Xu W, Zhou K. 2014 An Asymptotic Numerical Method for Inverse Elastic Shape Design. *ACM Transactions on Graphics (Proc. ACM SIGGRAPH'14)* **33**, 95:1–95:11.

[30] Albanesi AE, Pucheta MA, Fachinotti VD. 2013 A new method to design compliant mechanisms based on the inverse beam finite element model. *Mechanism and Machine Theory* **65**, 14 – 28.

[31] Pérez J, Thomaszewski B, Coros S, Bickel B, Canabal JA, Sumner R, Otaduy MA. 2015 Design and Fabrication of Flexible Rod Meshes. *ACM Transactions on Graphics (Proc. ACM SIGGRAPH'15)* **34**, 138:1–138:12.

[32] Kern M. 2002 Problèmes inverses : aspects numériques. Lecture.

[33] Derouet-Jourdan A, Bertails-Descoubes F, Thollot J. 2010 Stable Inverse Dynamic Curves. *ACM Transactions on Graphics (Proc. ACM SIGGRAPH Asia'10)* **29**, 137:1–137:10.

[34] Derouet-Jourdan A, Bertails-Descoubes F, Thollot J. 2011 3D inverse dynamic modeling of strands. In Wexler D, editor, *ACM SIGGRAPH 2011 Posters* p. Article No. 55 Vancouver, Canada. ACM SIGGRAPH ACM. Poster.

[35] Derouet-Jourdan A, Bertails-Descoubes F, Thollot J. 2013 Floating tangents for approximating spatial curves with G^1 piecewise helices. *Computer Aided Geometric Design* **30**.

[36] Ivanova E. 2000 On one approach to solving the Darboux problem. *Mechanics of Solids* **35**, 36–43.

[37] Love A. 1927 *A Treatrise on the Mathematical Theory of Elasticity*. Cambridge University Press.

[38] Langer J, Singer DA. 1996 Lagrangian Aspects of the Kirchhoff Elastic Rod. *SIAM Review* **38**, 605–618.

[39] Blumentals A. 2017 *Numerical modelling of thin elastic solids in contact*. PhD thesis Université de Grenoble Alpes.

[40] Derouet-Jourdan A, Bertails-Descoubes F, Daviet G, Thollot J. 2013 Inverse Dynamic Hair Modeling with Frictional Contact. *ACM Transactions on Graphics (Proc. ACM SIGGRAPH Asia'13)* **32**, 159:1–159:10.